K- and *W*-Band Free-Space Characterizations of Highly Conductive Radar Absorbing Materials

Nagma Vohra, *Student Member, IEEE*, and Magda El-Shenawee, *Senior Member, IEEE*

***Abstract*— This work presents a characterization technique of highly conductive material in the *K*- and *W*-bands. The transmission line theory model is modified to adapt to the phase challenges observed in the measured S-parameters at high frequency. The S-parameters measurements are obtained using the nondestructive focused beam free-space system connected with the network analyzer and the millimeter-wave frequency extenders. The system provides measurements in a frequency range from 5.8 to 110 GHz, and it includes focused beam horn lens antennas to minimize sample edge reflection. The thru-reflect-line (TRL) calibration and the time-gated feature of the network analyzer are used. Good agreement between the measured and calculated S-parameters in the transmission mode is achieved using the extraction algorithm. The measured S-parameters are further used to obtain the electromagnetic shield effectiveness parameters and the percentage of power absorbed in the material. In addition, the return loss of the metal-backed material is calculated using the extracted permittivity to obtain the maximum absorption at the desired frequencies.**

***Index Terms*— Free-space measurements, *K*- and *W*-band characterizations, material characterization, radar absorbing materials (RAMs), thru-reflect-line (TRL) calibration.**

I. Introduction

With the inclusion of radar systems in the automotive industry, the interest to manufacture radar absorbing materials (RAMs) has increased in recent years. Newly introduced car models are equipped with radar-based advanced driver assistance systems (ADAS), such as collision warning and collision avoidance (CW/CA), adaptive cruise control (ACC), assisted lane change, collision mitigation braking (CMS), and automated parking assist (APS), which provides high volume production with low-cost potential [1]. The radar sensors for these advanced systems are primarily deployed to function in the 24–26-GHz (short-range) and 76–77-GHz (long-range) allocated frequency bands [2]. The sensor at 77 GHz is typically much smaller, reducing the volume- and weight-related costs [3]. In addition, the long-range radar (LRR) systems at 77 GHz have shown improvement in many aspects from the short-range radars (SRRs) and mid-range radars (MRRs) [4], [5]. However, the deployment of ADAS systems has led to an increase in the number of automotive radar sensors operating simultaneously in a compact space. This results in signal interference that can lead to a reduced signal to noise ratio or ghost targets [6]. Furthermore, the coupling between transmit and receive antennas and the reflections from the adjacent metal structures of the vehicle can cause electromagnetic interference (EMI) in the automotive radar system.

Engineering and characterization of high-frequency RAMs have been investigated in the literature for years [7], [8]. In addition, the shielding from the EM waves depends on the critical properties of the engineered composite materials [9]–[11]. Therefore, the electromagnetic characterization of the RAM material versus frequency is of significant importance, i.e., obtaining the complex electric permittivity (ε) and complex magnetic permeability (μ). The literature is rich with reports on the aspect of material characterization [12]–[43]. These materials were characterized as lossy or low-loss materials, where a variety of extraction methods based on the measured S-parameters were reported [12]–[43].

In this work, we use the free-space characterization technique to measure the S-parameters with thru-reflect-line (TRL) as the calibration methods. While the electromagnetic characterization of lossless and low-to-moderate lossy materials is well-established in the literature, we focus here on characterizing highly conductive, inhomogeneous carbon-based materials in the *K*- and *W*-bands for the SRR and LRR radar systems, respectively. For example, among the samples handled in this work, sample P1 validates the success of the presented iterative extraction method where the obtained $\varepsilon'' = \sim 6$ in the *K*-band and ~ 4 in the *W*-band. Sample P2 demonstrates its potential use in the automotive industry as a radar-absorbing material where the absorption dip in the metal-backed measurements occurred in the *K*-band at 24 GHz after changing the thickness from 3.33 to 2.704 mm. Finally, sample P3 is different from the other two samples, demonstrating a very high-conductive material with ε'' values of ~ 100 and ~ 50 in the *K*- and *W*-bands, respectively. The proposed optimization technique, to find the initial guess values of the unknown relative permittivity, to be used in the extraction method highlights the novelty of this work. Our developed extraction algorithm is based on the transmission line theory [45], the iterative optimization algorithm [46], the modification due to configuration inhomogeneity in the *W*-band [15], and the inhomogeneity observation in 3-D metamaterial characterization, as reported

Manuscript received July 31, 2020; revised October 24, 2020; accepted November 19, 2020. Date of publication December 2, 2020; date of current version January 5, 2021. This work was funded in part through the GAP Chancellor's Innovation Fund under Award 003184-00001A and in part by the Department of Electrical Engineering at the University of Arkansas. The RAM samples were provided by a company under a nondisclosure agreement. The Associate Editor coordinating the review process was Sasan Bakhtiari. *(Corresponding author: Nagma Vohra.)*

The authors are with the Department of Electrical Engineering, University of Arkansas, Fayetteville, AR 72701 USA (e-mail: nvohra@uark.edu; magda@uark.edu).

Digital Object Identifier 10.1109/TIM.2020.3041821

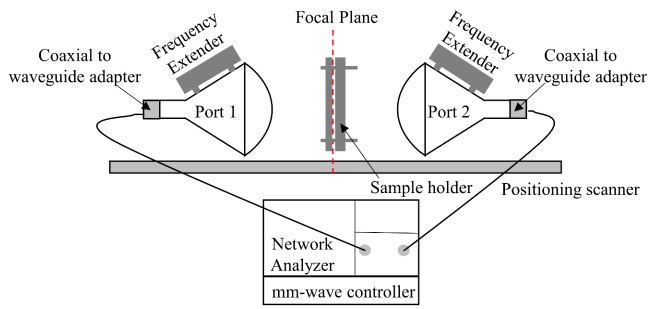

Fig. 1. Microwave and millimeter-wave free-space measurement system.

in [48]. The proposed method provides the correct extraction of the relative permittivity of highly conductive samples measured in both the K- and W-bands. In addition, the extracted complex permittivity is further used to calculate the metal-backed return loss at several estimated sample thicknesses to obtain the maximum absorption at 24 and 77 GHz for use in the SRR and LRR systems, respectively. We present the percentage of power absorbed and the shielding effectiveness (SE) of materials, calculated based on the measured S-parameters. To the best of our knowledge, this is the first time that this extraction method has been investigated for microwave and millimeter-wave characterizations of highly conductive RAM samples measured using the free-space method.

A total of 51 RAM samples were characterized under a nondisclosure agreement. Preliminary results to validate the method with commercial RAM materials were reported in our conference papers [28], [49], where materials of 1- and 2-mm thicknesses were purchased from the ARC Technology Inc.

The free-space system is described in Section II, the TRL calibration in Section III, the model formulations in Section IV, the experimental results in Section V, and the conclusion in Section VI. The Appendix describes the time gating feature used in the measurements, in addition to presenting the 3-dB beamwidth of the system in the K- and W-bands.

II. Free-Space System Setup

The microwave and millimeter-wave free-space measurement system is sketched in Fig. 1. It is composed of transmitting and receiving conical lens horn antennas with bandwidth from 5.8 to 110 GHz, a sample holder, an Agilent PNA E8361C network analyzer, an N5260A millimeter-wave controller, and two millimeter-wave frequency extenders. The antennas and the sample holder are mounted on a positioning scanner fixed on a large aluminum table in the XZ plane. This positioning system provides four degrees of freedom for the antenna movement in the X, Z, elevation angle (theta), and azimuth angle (phi) directions with a precision of ± 2 μm [39], [40]. The sample holder stage provides motion in the Y-direction only.

In order to focus the antenna beam on the sample center, two equal planoconvex dielectric lenses are mounted back-to-back in the conical horn antenna. The distance between the two antennas is $\sim$61 cm, and the focal distance to the diameter ratio of the lens is unity, with the lens's diameter equal to $\sim$30.5 cm. Thus, the dielectric lens focuses the beam incident on a sample at a specific frequency to a footprint of diameter approximately one wavelength [39]. The 3-dB beamwidths in the K- and W-bands are $\sim$1.2 cm and 4 mm, respectively (see Fig. 11). A custom-made sample holder is placed at the common focal plane of both antennas. It holds the sample under test between the two antennas such that the focal point of port 1 antenna is at the front face of the sample and that of port 2 antenna is at the back face of the sample. The sample holder is made of acrylic material and can hold the samples of size $6'' \times 6''$ and $12'' \times 12''$.

The PNA E8361C network analyzer provides frequencies from 10 MHz to 67 GHz using 1.85-mm female coaxial cables from the network analyzer to the rest of the system. A coaxial to waveguide adapter is used to feed the antennas. These adapters are designed for the specific frequency ranges at which only the TE_{10} dominant mode is excited [33]. A total of eight pairs of the coaxial to waveguide adapters cover the frequency range from 5.8 to 110 GHz. In this work, the coaxial to waveguide adapters of the K-band (1.85-mm female connector) and the W-band (1-mm female connector), purchased from Keysight Technologies (W281C for the W-band and K281C for the K-band), are used. For the frequency bands up to 67 GHz, the horn antennas are directly connected to the network analyzer, whereas, for the frequency bands higher than 67 GHz, the horn antennas are connected to the millimeter-wave frequency extenders, which provides frequencies ranging from 67 to 110 GHz.

The same conical horn lens antennas can be used for the entire range from 5.8 to 110 GHz. However, the appropriate coaxial to waveguide adapter that connects the network analyzer to the horn antenna is replaced for each desired bandwidth.

III. Free-Space Calibration and Measurement Procedures

A. System Calibration

The electromagnetic characterization of materials depends on the correct measurement of its complex S-parameters. To account for measurement errors in cables and network analyzer, a calibration procedure is needed. Among many well-known two-port calibration techniques [35], [38], [44], the TRL is considered the most appropriate technique for the free-space measurements [15], [28], [39]. The calibration steps are summarized in the following (see Fig. 2).

1) THRU standard in the TRL calibration is implemented by keeping both port 1 and port 2 antennas at their home positions and taking the measurements through the air. Here, the incident beams from both antennas are focused on the reference plane marked as the red dotted line in Fig. 2. This selected reference plane is the common focal plane of both antennas with a focal distance of $\sim$305 mm, as shown in the figure.
2) REFLECT standard is implemented by placing a gold-plated plate (also known as the gold-plated mirror) of thickness $D = 6.35$ mm in the sample holder. The mirror in the sample holder is placed at the common focal plane of the two antennas. Thus, the golden mirror side facing port 1 antenna is aligned with the reference plane,

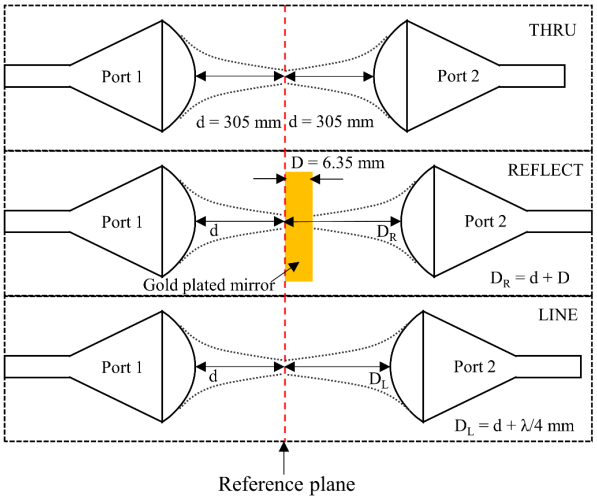

Fig. 2. TRL calibration procedure for the free-space measurement system.

i.e., the incident beam from the port 1 antenna is focused on the air–gold mirror interface. However, due to the thickness of the gold mirror, port 2 antenna is moved back by a distance $D_R = d + D$ from the reference plane, and the measurement of the reflect standard is recorded.

3) LINE standard is implemented by removing the gold mirror from the sample holder and positioning port 2 antenna at a distance of $D_L = d + \lambda/4$ from the reference plane. Here, $\lambda/4$ distance is calculated at the mid-frequency band, and the measurement through the air is recorded.

In order to verify the correctness of the calibration, S_{11} and S_{22} of a gold-plated plate are measured. The measurement is obtained by moving the port 2 antenna back by the distance $D_R = d + D$ from the reference plane, as described in step 2 of the TRL calibration. The threshold of the S_{11} and S_{22} magnitudes should be within ± 0.1 dB, and the phase should be within 2° from $\pm 180°$. If these conditions are not achieved, the calibration is repeated.

B. Free-Space Measurements

In this work, two types of measurements are conducted: transmission mode and metal-backed reflection mode. As known, the measurements are sensitive to the thickness accuracy of the samples. Here, the sample thickness is measured at ten different points on the sample, and their average ($D = D_{\text{ave}}$) is considered the sample thickness. The measurements of ten points are acquired using the Mitutoyo Digimatic micrometer mounted on a flat granite stand. The sample is placed in the holder, while the incident beam from port 2 antenna is focused on the air–sample interface by positioning it back by the distance $(d+D)$ from the reference plane. The four complex S-parameters—S_{11}, S_{21}, S_{12}, and S_{22}—are measured and recorded using the network analyzer. For the metal-backed reflection mode, the sample is placed in the holder and backed with a gold-plated plate of 6.35-mm thickness. The front face of the sample is facing port 1 antenna, aligning with the reference plane, and only the S_{11} parameter is measured.

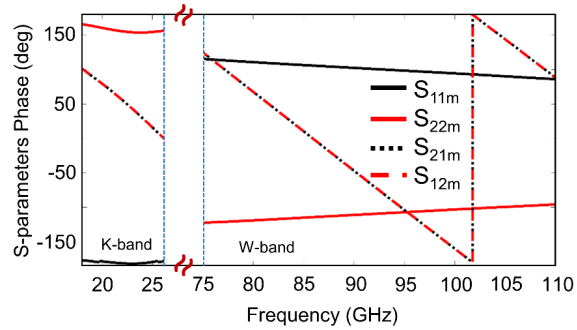

Fig. 3. Measured S-parameters phase of sample P1 in the *K*- and *W*-bands.

All results of this work are obtained using the time-gated feature of the network analyzer (see the Appendix for details).

IV. Extraction Method

A. Transmission Line Model

The concept of the extraction method to obtain the complex relative permittivity is based on the transmission line theory [45], [46]. However, our material samples have an unusual level of inhomogeneity and conductivity that necessitated additional work to accurately extract the complex relative permittivity $\hat{\varepsilon_r} = \varepsilon' - j\varepsilon''$ with $\varepsilon'' = \sigma/\omega\varepsilon_o$, where σ is the conductivity of the material, ω is the angular frequency of the incident beam, and ε_o is the free-space permittivity. The reflection coefficient and transmission coefficients are [45]

$$\Gamma = \frac{Z_S - Z_o}{Z_S + Z_o} = \frac{\sqrt{\frac{\hat{\mu_r}}{\hat{\varepsilon_r}}} - 1}{\sqrt{\frac{\hat{\mu_r}}{\hat{\varepsilon_r}}} + 1}, \quad T = e^{-j\omega\sqrt{\varepsilon^*\mu^*}D} \tag{1}$$

where Z_o is the characteristic impedance of air, Z_S is the characteristic impedance of the material, $\varepsilon^* = \varepsilon_o\hat{\varepsilon_r}$, and D is the thickness of the sample under test. For nonmagnetic materials, the magnetic permeabilities are $\hat{\mu_r} = 1$ and $\mu^* = \mu_o$.

The extraction method reported in [46] is based on iteratively minimizing error functions between the S-parameters measurements and calculations in each iteration. However, the literature reported that this method has some challenges in inhomogeneous configurations [15], [48]. In [15], the work in the *W*-band reported inhomogeneity in the configuration due to the antennas' movement, while the tested samples were lossless or of low-loss homogeneous materials. In [48], the work reported inhomogeneity due to the inclusion of the metamaterial cells. In both works, the iterative method was slightly modified. In this study, we observed that the samples are inhomogeneous in the *W*-band due to both factors, i.e., antennas' movements and mixing several ingredients at specific percentages (e.g., carbon, fiber, and nylon). Note that the RAM industry aims at engineering highly absorbing radar materials by adding carbon-based ingredients. The discussed challenge is demonstrated in Fig. 3 in the *W*-band and not the *K*-band. The phase of S_{11} is not equal to the phase of S_{22}, while the phases of S_{21} and S_{12} are equal. This phase difference prohibits the minimization of the error functions between the measured and calculated S-parameters to provide accurate values of the extracted permittivity. The magnitude

of the measured S-parameters is almost the same with some small differences due to measurement accuracy. As a result, we modified the model to combine the methods reported in [15], [45], and [46] in the W-band while keeping the same model of [46] in the K-band.

Thus, the novelty of this work lies in the proposed optimization technique that demonstrates the significance of the initial values of the unknown permittivity for such highly conductive materials in both the K- and W-bands. To find these initial guess values, the error functions to be minimized in the K-band are

$$\mathrm{Fun}_1 = 10 * \log_{10}|S_{11m} - S_{11c}| \tag{2a}$$
$$\mathrm{Fun}_2 = 10 * \log_{10}|S_{21m} - S_{21c}| \tag{2b}$$
$$\mathrm{Fun}_3 = 10 * \log_{10}|S_{12m} - S_{12c}| \tag{2c}$$
$$\mathrm{Fun}_4 = 10 * \log_{10}|S_{22m} - S_{22c}| \tag{2d}$$

where, in the W-band, we minimize the following functions:

$$\mathrm{Fun}_1 = 10 * \log_{10}|S_{21m} - S_{21c}| \tag{3a}$$
$$\mathrm{Fun}_2 = 10 * \log_{10}|S_{12m} - S_{12c}| \tag{3b}$$
$$\mathrm{Fun}_3 = 10 * \log_{10}||S_{11m}| - |S_{11c}|| \tag{3c}$$
$$\mathrm{Fun}_4 = 10 * \log_{10}||S_{22m}| - |S_{22c}|| \tag{3d}$$

where S_{11m}, S_{22m}, S_{21m}, and S_{12m} are the measured complex transmission parameters, and $S_{11c} = (\Gamma(1 - T^2))/(1 - \Gamma^2 T^2)$ and $S_{21c} = (T(1-\Gamma^2))/(1-\Gamma^2 T^2)$ are the calculated complex parameters at each iteration in the minimization search using the equation in [46]. Theoretically, $S_{22c} = S_{11c}$, and $S_{12c} = S_{21c}$. Note that the error functions in (2a)–(2d), (3a), and (3b) minimize both the amplitude and phase of the parameter, while the functions in (3c) and (3d) minimize only the magnitude of the parameter.

B. Absorption in Transmission and Metal-Backed Modes

The main interest of the RAM industry is to examine the absorption of the material in transmission and when the material covers a metallic target. In the transmission mode, the amount of power absorbed, reflected, and transmitted through the sample is obtained using the measured S-parameters as follows:

$$\frac{\text{Power reflected}}{\text{Power incident}} = |S_{11m}|^2 \tag{4a}$$
$$\frac{\text{Power transmitted}}{\text{Power incident}} = |S_{21m}|^2 \tag{4b}$$
$$\frac{\text{Power absorbed}}{\text{Power incident}} = 1 - |S_{11m}|^2 - |S_{21m}|^2. \tag{4c}$$

For the metal-backed reflection, $S_{11\mathrm{refc}}$ is given by [13]

$$S_{11\mathrm{refc}} = \frac{\sqrt{\frac{\hat{\mu}_r}{\hat{\varepsilon}_r}}\tanh\left(j\omega\sqrt{\varepsilon^*\mu^*}D\right) - 1}{\sqrt{\frac{\hat{\mu}_r}{\hat{\varepsilon}_r}}\tanh\left(j\omega\sqrt{\varepsilon^*\mu^*}D\right) + 1} \tag{5}$$

where D is the sample thickness, and $\varepsilon^* = \varepsilon_o\hat{\varepsilon}_r$, $\mu^* = \mu_o\hat{\mu}_r$, and $\hat{\mu}_r = 1$ for nonmagnetic materials. The $S_{11\mathrm{refc}}$ is measured upon backing the sample with the gold mirror and is also calculated using the extracted complex permittivity $\hat{\varepsilon}_r$.

C. Electromagnetic Shield Effectiveness

The electromagnetic shield effectiveness (SE) is defined by the ability of a material to attenuate the intensity of electromagnetic radiation to an adequate level desired based on the application. The total SE is the summation of the reflection, absorption, and multiple internal reflection losses at the air–sample interface. When SE_A is $\geq$10dB, the multiple internal reflections is negligible, which is usually the case. Therefore, the total SE is expressed by [47]

$$\mathrm{SE} = \mathrm{SE}_A + \mathrm{SE}_R \tag{6a}$$

where SE_A and SE_R are the absorption and reflection shieldings, given as functions of the S-parameters by

$$\mathrm{SE}_A = -10\log_{10}\left(\frac{|S_{21m}|^2}{1 - |S_{11m}|^2}\right) \tag{6b}$$
$$\mathrm{SE}_R = -10\log_{10}\left(1 - |S_{11m}|^2\right). \tag{6c}$$

The SE depends on the frequency of the excitation, the thickness of the sample, the material composite, and the fabrication and processing conditions [9].

V. Experimental Results

In this section, we present the results of three samples in both the K- and W-bands. While the developed method is applicable to magnetic and nonmagnetic materials, all samples presented here are assumed nonmagnetic, based on information from the manufacturer. The samples are referred to by P1, P2, and P3 and are made of highly conductive materials with an average thickness of around 3 mm. For each sample, the extracted complex relative permittivity, the magnitude validation of S-parameters (dB), and the return loss (dB) are presented versus frequency. The SE and the percentage of power absorbed for each sample are also presented in both the K- and W-bands.

A. Initial Guess

While, in the K-band, the initial guess in the iterative solver for the complex relative permittivity can start with $(1 - j0)$, which is more involved in the W-band, the simplest method to select the initial guess of the material in the W-band is to use the values extracted at 26.5 GHz in the K-band. Another method to select the initial guess in the W-band is to map the roots of error functions in (3) individually and select those that are close to each other. The initial guess is used in a line search using the MATLAB code, and the algorithm stops when a preassigned threshold error is achieved. In order to validate the extracted permittivity, the error between the calculated and measured S-parameters is obtained, and the results are selected based on the minimum error. In some cases, all initial guess values provide the same solutions. Fig. 4 demonstrates the map of the roots of (3a), (3c), and (3d) for sample P1. Table I lists various initial guess values used in the line search of the W-band solution. The listed values of the initial guess converged to the same solution of the extracted permittivity that is shown in Fig. 5(a), except for a couple of initial guess points. For example, the first point marked as 1

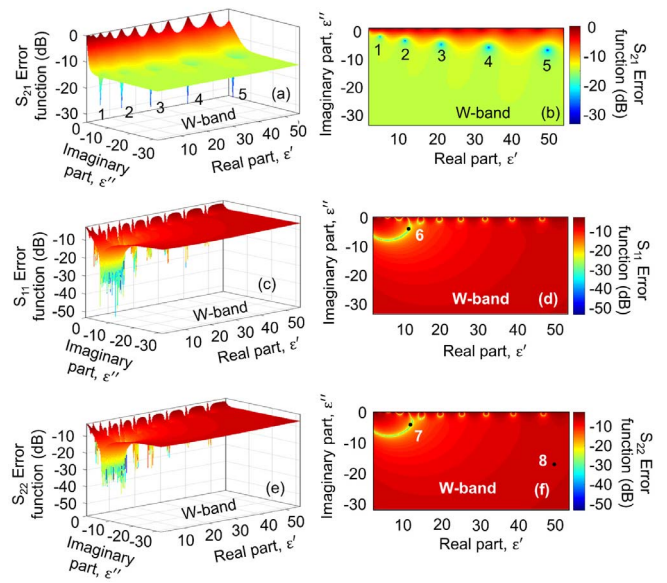

Fig. 4. Initial guess in the *W*-band for sample P1. (a) 3-D Error function showing the minimum error between $S_{21\text{measured}}$ and $S_{21\text{calculated}}$. (b) Top view of (a). (c) 3-D error function graph showing minimum error between $|S_{11}|_{\text{measured}}$ and $|S_{11}|_{\text{calculated}}$. (d) Top view of (c). (e) 3-D error function graph showing minimum error between $|S_{22}|_{\text{measured}}$ and $|S_{22}|_{\text{calculated}}$. (f) Top view of (e).

TABLE I

SAMPLE P1—INITIAL GUESS POINTS BASED ON S_{21}, S_{11}, AND S_{22} ERROR FUNCTIONS

W-band			
Number	Initial Guess		Extracted Permittivity Solution
	ε'	ε''	
K-band	12.98	4.65	Same as Fig. 5a
1	4.1	2.8	Wrong S-parameter
2	11.1	4.1	Same as Fig. 5a
3	21.3	5.2	Same as Fig. 5a
4	34.7	6.2	Same as Fig. 5a
5	51.4	7.2	Same as Fig. 5a
6	11.1	4.1	Same as Fig. 5a
7	11.6	4.1	Same as Fig. 5a
8	52.8	18.9	Ambiguous

with ($\varepsilon' = 4.1$ and $\varepsilon'' = 2.8$) gave a wrong validation when comparing the measured and calculated S-parameters with a difference of ~25–30 dB in the S_{21} parameter. The second point marked by 8 ($\varepsilon' = 52.8$ and $\varepsilon'' = 18.9$) was a random point in the considered space, giving an ambiguous solution of the permittivity. This means that the values of the real and imaginary parts demonstrate jumps in a stepwise manner at certain frequencies similar to what was reported in [50] and [51]. Therefore, the solutions based on these two initial guesses were rejected, and the converged solution with the good S-parameter validations was selected.

B. Electrical Properties

The extracted permittivity of P1 sample is shown in Fig. 5(a); the validation of the S-parameters is shown in Fig. 5(b) for the *K*- and *W*-bands. The solid black line represents the real part, and the red solid line represents the imaginary part of the extracted permittivity in Fig. 5(a). The large values of ε'' across the *K*- and *W*-bands demonstrate

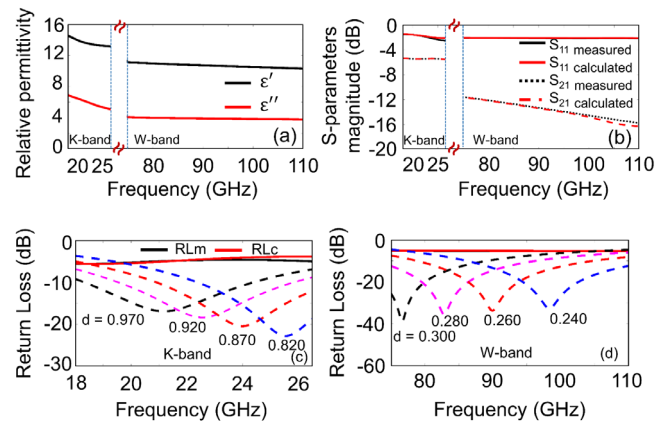

Fig. 5. (a) and (b) Results of sample P1 in *K*- and *W*-bands. (a) Relative permittivity plot showing real and imaginary parts ε' and ε'', respectively. (b) Comparison between the measured and calculated S-parameters magnitudes. (c) and (d) Return loss of metal-backed material of Sample P1. (c) Measured and calculated return loss for the metal-backed reflection measurement at different thicknesses in the *K*-band. (d) Measured and calculated return loss for the metal-backed reflection measurement at different thicknesses in the *W*-band.

the high conductivity of the material. The relative permittivity of P1 shows a decreasing trend in the *K*-band as the frequency increases, where, in the *W*-band, it is almost constant versus frequency with an average value of 10.67 for ε' and that of 3.89 for the ε''. The extracted relative permittivity of P1 in both *K*- and *W*-bands is further used to calculate the S-parameters, as shown in Fig. 5(b). A maximum difference observed between the magnitudes of calculated and measured S_{11} (red solid and black lines, respectively) is 0.51 dB and that between calculated and measured S_{21} (dashed red and black dotted line, respectively) is 0.001 dB in the *K*-band. On the other hand, in the *W*-band, the error is 0.026 and 0.8 dB between the calculated and measured S_{11} and S_{21}, respectively. This demonstrates a good validation of the extraction model for sample P1.

C. Return Loss for Metal-Backed Material

The return loss for sample P1 is obtained versus frequency in the *K*- and *W*-bands, as presented in Fig. 5(c) and (d), respectively. The red solid and black lines in Fig. 5(c) and (d) represent the measured and calculated return loss values obtained at the average thickness of the sample (3.153 mm). An approximate maximum error of the 1.0-dB difference between the calculated (red solid line) and measured return loss (solid black line) is observed at a 26.5-GHz frequency in Fig. 5(c), whereas, it is ~0.001 dB at 110.0 GHz in Fig. 5(d). More importantly, with the sample thickness of 3.153 mm, there was no observed resonance in the measured return loss at any frequency in the *K*- or *W*-band. Upon using the extracted complex permittivity in (5) with different thicknesses, the sample can demonstrate resonance if made of different thicknesses. The calculated return loss at four other thicknesses is shown in Fig. 5(c) for the *K*-band and Fig. 5(d) for the *W*-band (see dotted colored lines). In the *K*-band figure, the black dotted, magenta, red, and blue lines in Fig. 5(c) represent return loss calculated at a thickness

TABLE II

CALCULATED ABSORPTION VALUES USING NEW THICKNESS SHOWN IN FIG. 5(c) AND (d)

Number	K-band			W-band		
	Thickness (mm)	Max. Absorption frequency (GHz)	Bandwidth (GHz)	Thickness (mm)	Max. Absorption frequency (GHz)	Bandwidth (GHz)
1 --	0.970	21.15	6.05	0.300	77	22.39
2 --	0.920	22.56	6.27	0.280	82.83	23.78
3 --	0.870	24.0	6.42	0.260	89.94	25.99
4 --	0.820	25.55	6.53	0.240	98.32	28.46

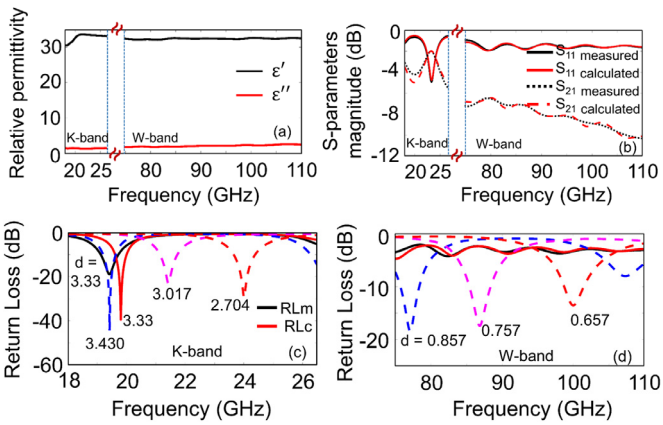

Fig. 6. Results for sample P2 in the K- and W-bands. (a) Real and imaginary parts of permittivities, ε' and ε'', respectively. (b) Comparison between the measured and calculated S-parameters magnitude. (c) and (d) Measured and calculated metal-backed return loss at different thicknesses in (c) K-band and (d) W-band.

of 0.970, 0.920, 0.870, and 0.820 mm, respectively. Similarly, for the W-band, the black dotted, magenta, red, and blue lines in Fig. 5(d) represent the return loss calculated for 0.300, 0.280, 0.260, and 0.240 mm, respectively. In addition, the data in Table II show the frequency at which the maximum absorption occurs for each thickness and the bandwidth at -10 dB. The table indicates that the obtained bandwidth in the K-band is $\sim$6 GHz at each thickness, whereas it is more than 20 GHz in the W-band. Furthermore, it can be observed from Fig. 5(c) and (d) and Table II that, for a small change in the sample thickness of $\sim$50 μm, in the K-band and $\sim$20 μm in the W-band, the resonance shifts by $\sim$1.5 and $\sim$5.0 GHz, respectively. Thus, to use the sample material as an absorber for radar systems, it is imperative to manufacture the sample at the correct thickness of the needed frequency. For example, in the automotive industry, the use of 24 GHz in short range and 77 GHz in LRR detection units is commonplace with the advent of environment object detection technologies being deployed in all high-tech automobiles. To utilize sample P1 as an absorber in these SRR and LRR systems, it has to be manufactured precisely at a thickness equal to 0.870 and 0.3 mm, respectively.

The results of the second sample P2 are shown in Fig. 6. This sample has an average thickness of 3.33 mm. Similar to sample P1, the initial guess of the complex permittivity is selected using the solution of the K-band validated by selecting the initial guess based on the error functions of (3). The results are not shown here due to space limitations. The extracted results of the complex permittivity are shown in Fig. 6(a). The solid black line in Fig. 6(a) represents the real part of the permittivity, and the red solid line represents the imaginary part. The real part demonstrates an increasing trend until around 22 GHz and then shows an almost constant value of $\sim$34 in the K-band. For the W-band, it shows an almost constant value with an average of 32.46 for ε' and that of 2.11 for ε''.

In order to validate the permittivity solution, the S-parameters are calculated using the extracted permittivity values in the K- and W-bands and compared with measurement magnitudes. A maximum difference in S_{11} was observed to be 0.16 dB and in S_{21} to be 0.76 dB in the K-band, while it is 0.2 and 0.36 dB in the W-band, as shown in Fig. 6(b). The results demonstrate a good validation of the extraction model in both K- and W-bands for this sample, consistent with sample P1.

The metal-backed return loss (dB) is shown in Fig. 6(c) and (d), for the K- and W-bands, respectively. The red solid and black lines in Fig. 6(c) and (d) represent the measured and calculated return loss values obtained at the actual average sample thickness of 3.33 mm. Unlike other samples discussed earlier, the measured return loss of this sample (solid black line) indicates the maximum absorption of the signal at 19.42 GHz, as shown in Fig. 6(c). This sample demonstrates a narrow band absorber providing a bandwidth of $\sim$600 MHz at 19.42 GHz. A shift of approximately 400 MHz from the measured maximum absorption is observed in the calculated return loss (red solid line) obtained at the same sample thickness (3.33 mm). This shift could be due to a slight change in the sample thickness when the measurements are performed. As described earlier, our method of taking the sample thickness is based on measuring the thickness at ten different points on the sample and averaging them. It is likely that, when the measurements are performed, the spot on the sample at which the beam hits has a slightly different thickness than the average thickness used in the algorithm. In addition, as observed earlier in this section, a slight change of $\sim$50 μm in the thickness caused the resonance to shift significantly. To prove this, the return loss for this sample is calculated at the sample thickness of 3.43 mm (a change of 0.1 mm), which shifted the maximum absorption back at the same 19.42-GHz frequency (blue dotted line) of the measured return loss, as shown in Fig. 6(c). The return loss is also calculated at the other two thicknesses, -3.017 and 2.704 mm, which displays the maximum absorption at 21.43 and 24 GHz, as shown in magenta dotted and red lines in Fig. 6(c), respectively.

The return loss for sample P2 in the W-band is presented in Fig. 6(d). At high frequencies, multiple reflections are observed, as shown in the figure. However, the calculated metal-backed return loss (red solid) follows the same behavior as the measured one (solid black line), demonstrating a maximum difference of $\sim$0.76 dB at 75 GHz. This validates the extraction method for this sample. In addition, in Fig. 6(d), the blue dotted, magenta, and red lines represent the metal-backed return loss calculated, using the extracted permittivity and sample thicknesses of 0.857, 0.757, and 0.657 mm,

TABLE III

MEASURED AND CALCULATED ABSORPTION AT ACTUAL AND NEW SAMPLE THICKNESSES SHOWN IN FIG. 6(c) AND (d)

Number	K-band			W-band		
	Thickness (mm)	Max. Absorption frequency (GHz)	Bandwidth (GHz)	Thickness (mm)	Max. Absorption frequency (GHz)	Bandwidth (GHz)
Measured and calculated absorption at the actual sample thickness						
RLm	3.330	19.42	0.6	3.330	-	-
RLc	3.330	19.82	0.380	3.330	-	-
Calculated absorption using new thickness						
1	3.430	19.42	0.420	0.857	77	2.62
2	3.017	21.43	0.580	0.757	86.86	2.84
3	2.704	24.0	0.730	0.657	99.88	2.91

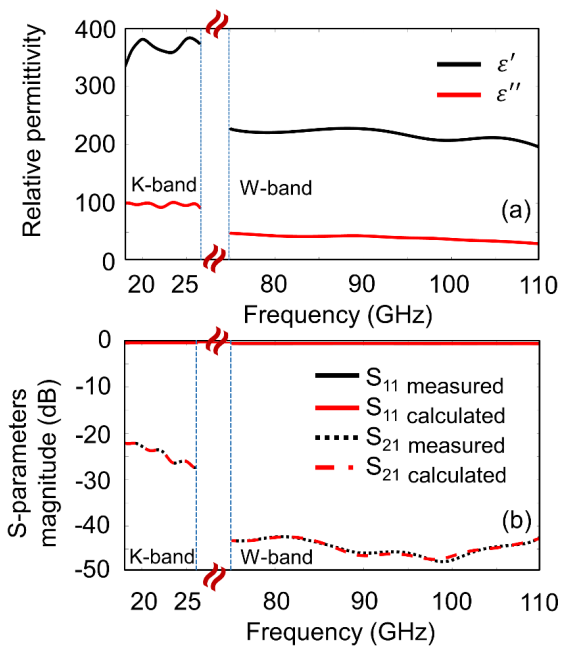

Fig. 7. Results of sample P3 in the K- and W-bands. (a) Real and imaginary parts of the relative permittivities, ε' and ε'', respectively. (b) Comparison between the measured and calculated S-parameters magnitudes.

respectively. Table III lists the frequency of the maximum absorption at each of these thicknesses and the bandwidth obtained using the -10-dB threshold. To utilize sample P2 as an absorber in the SRR and LRR systems, it has to be manufactured precisely at a thickness equal to 2.704 and 0.857 mm, respectively.

The results of the third sample, P3, are shown in Fig. 7, where the average thickness of the sample is 3.373 mm. This sample represents the highest conductive material among all the 51 samples characterized in this project. Here, the error functions of (3a) and (3b) were modified to be similar to (3c) and (3d) where the phase minimization was removed and only the error in magnitudes was used. Here, even in the K-band, the initial guess is marked as 1 where ($\varepsilon' = 1$ and $\varepsilon'' = 0$), provided a negative value of the real part of $\hat{\varepsilon_r}$, as listed in Table IV. The same for the random initial guess is marked by 7 ($\varepsilon' = 6$ and $\varepsilon'' = 10.3$). All other initial guess values obtained from the error functions converged to the same solution that also provided good comparisons between the calculated and measured S-parameter magnitudes,

TABLE IV

SAMPLE P3—INITIAL GUESS POINTS BASED ON S_{21}, S_{11}, AND S_{22} ERROR FUNCTIONS

K-band			
Number	Initial Guess		Extracted Permittivity Solution
	ε'	ε''	
1	1	0	Negative ε': rejected
2	44.6	50.2	Same as Fig. 7a
3	288	93.4	Same as Fig. 7a
4	329	97	Same as Fig. 7a
5	483	113.6	Same as Fig. 7a
6	585	147	Same as Fig. 7a
7	6	10.3	Negative ε': rejected

as shown in Fig. 7. Here, the initial guess of the permittivity in the W-band is obtained from the solution in the K-band at 26.5 GHz.

The results of the extracted permittivity are shown in Fig. 7(a) for the K- and W-bands. The black solid line represents the real part, and the red solid line represents the imaginary part. The comparison between the measured and calculated S-parameters magnitudes is shown in Fig. 7(b) with the solid lines representing S_{11} and the dashed or dotted lines representing S_{21}. It is observed that the real and imaginary parts of the extracted permittivity in Fig. 7(a) are noticeably higher in the K-band compared with those in the W-band. This observation is consistent with samples P1 and P2 results but with less difference between the two bands. We also note wavy plots in the permittivity versus frequency consistent with the P2 sample results. This behavior could also be due to the multiple reflections in the sample. In Fig. 7(b), the sample P3 is highly reflective due to its high conductivity, demonstrated in the permittivity imaginary parts in Fig. 7(a). The magnitude of S_{11} is in the range between -1 and $\sim$0 dB in the K- and W-bands, while that of S_{21} is between ~-20 and ~-30 dB in the K-band and between ~-40 and ~-50 dB in the W-band.

The maximum difference observed between the magnitudes of calculated and measured S_{11} and S_{21} is 0.01 dB in the K-band, as shown in Fig. 7(b), whereas it is 0.012 and 0.86 dB between the calculated and measured S_{11} and S_{21}, respectively, in the W-band. Even with almost no transmission through this sample, the difference between the measured and calculated S-parameters is less than 1 dB, proving the validity of this extraction model for highly conductive materials.

For the metal-backed configuration, this sample proved to be unsuitable as a RAM. The return loss results (not included) did not show absorption in the mm-range of sample thickness. However, it is possible to use this material as absorbing thin film covering metallic targets, where thicknesses of less than 50 μm were observed to provide absorption of fewer values ~-12 dB at 110 GHz.

D. Absorption and Shield Effectiveness

The percentage of power absorbed in the transmission mode is obtained using (4c). A comparison between the three samples is shown in Fig. 8. Sample P1 demonstrates higher

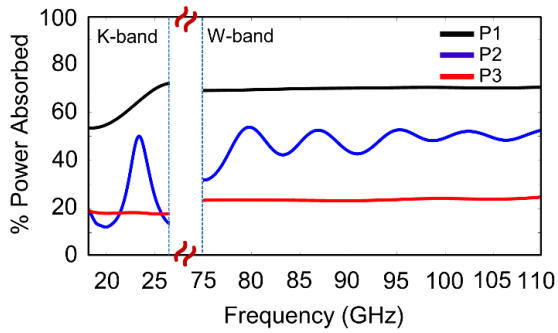

Fig. 8. Percentage power absorbed based on measured S-parameters in samples P1, P2, and P3 obtained in the K- and W-bands.

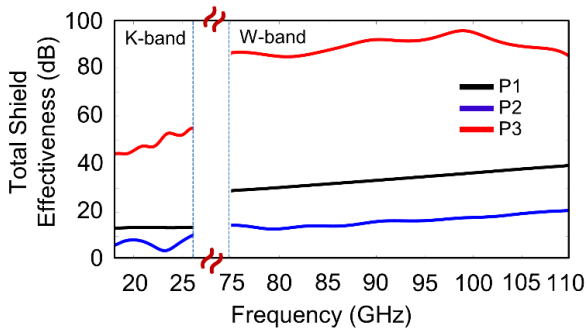

Fig. 9. Electromagnetic total SE based on the measured S-parameters of samples P1, P2, and P3.

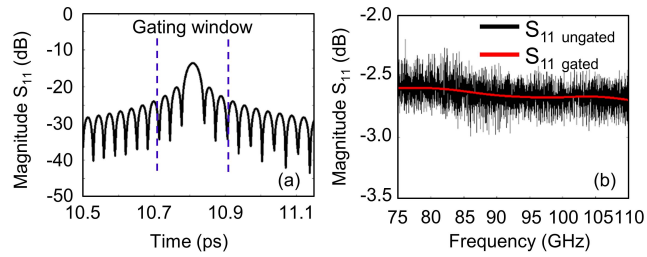

Fig. 10. Time-domain gating on the S_{11} data of sample P1 obtained in the W-band. (a) Inverse Fourier transformed time-domain S_{11} magnitude showing the applied gating window using the network analyzer gating feature. (b) Ungated (black solid line) and gated (red solid line) S_{11} magnitude (dB).

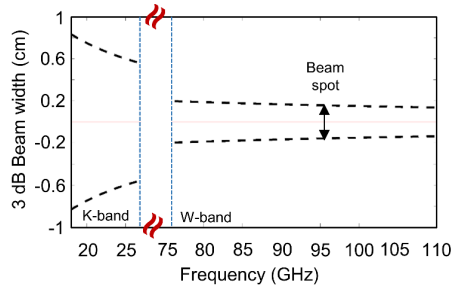

Fig. 11. Plot for 3-dB beamwidth of the incident beam on the sample under test across the whole K- and W-bands.

absorption values compared with that in samples P2 and P3. This behavior is consistent with the extracted permittivity of these materials.

A comparison of the total SE of the three samples, obtained using (6a), is shown in Fig. 9. The value of SE (total SE) is the sum of SE_A (absorption SE) and SE_R (reflection SE). Due to space limitations, we omitted the results of SE_A and SE_R and presented only the SE values in Fig. 9. As observed in the results, the SE is higher in the W-band than in the K-band in all three samples. In addition, as the frequency increases, the SE increases, except for P3 in the W-band, where it shows wavy behavior versus frequency. P3 shows higher SE values than that of P1, followed by P2. Furthermore, a wavy behavior in the SE plots observed in samples P2 and P3 is consistent with their extracted permittivity and also with the literature [9] for carbon-based nanostructured polymeric materials. The work in [9] described such behavior as the irregular nature of the included conductive materials.

VI. Conclusion

We presented the results of the free-space characterization method for three highly conductive nonhomogeneous carbon-based RAM samples. The TRL calibration was utilized here, and the measurements were conducted in the K- and W-bands. The developed method is based on an iterative optimization model to extract the complex permittivity of the engineered materials. The initial guess technique and the extraction algorithm that we presented in this article have successfully provided the correct relative permittivity of highly conductive samples (e.g., sample P3). The validation of the extracted permittivity was based on minimizing the error between the measured and calculated S-parameters. The S-parameters calculations were based on using the extracted complex permittivity in the S-parameters expressions of the transmission line model [45]. In all samples, the maximum error was less than 1 dB. Furthermore, a validation was demonstrated for the metal-backed samples based on a minimum error between the measured and calculated return loss.

The phase difference between the S_{11} and S_{22} parameters in the measurements using the TRL calibration was reported in the literature in the W-band [15] and the Ku-band [48]. We observed the same issue, particularly for the high-conductive materials considered here. These phase discrepancies represented a challenge when using the original extraction methods in [45] and [46] as it has led to ambiguous solutions similar to those reported in [50] and [51] or to incorrect validation of the measured and calculated S-parameters, as discussed in Section V.

Here, we modified the extraction method by simultaneously minimizing the functions of the S-parameters based on their magnitude and also generating a pool of initial guesses based on the individual error functions. Otherwise, it would have been almost impossible for the W-band measurements to start the optimization algorithm with an initial guess as $\varepsilon' = 1$ and $\varepsilon'' = 0$ (similar to the K-band). Therefore, we adopted a similar technique to that reported in [15] to obtain the initial guess in the W-band, as presented in Fig. 4.

The results also show that using metal-backed samples does not necessarily demonstrate resonances at the desired frequency. However, the extracted complex permittivity can be utilized to design the appropriate thickness of the sample in order to obtain the maximum resonance in the return loss at the desired frequency. In addition, the total SE and the percentage of power absorbed in the transmission mode were obtained to

guide the selection of the appropriate material, in particular at 24 and 77 GHz, for the automotive radar application.

APPENDIX

Upon measuring the S-parameters, the time gating is implemented on the raw data. This feature in the network analyzer helps remove the postcalibration errors caused by the reflection of the sample's edge and load impedance mismatch due to any imperfection in the calibration standards. Here, we show the raw and gated data of S_{11} of the metal-backed reflection mode of sample P1, as an example, in Fig. 10. First, the inverse Fourier Transform of the frequency-domain S_{11} raw data is obtained, as shown in Fig. 10. Then, the gating window is applied to the time-domain transformed data that include the main lobe and two side lobes. The gated time-domain data are transformed back to the frequency domain using the Fourier transform, as shown in the figure (red curve). An additional advantage of the gating is removing the noise. This procedure is applied to all S-parameters measured in this work.

The 3-dB beamwidth across the K- and W-bands is presented in Fig. 11, where the distance between the two dashed lines represents the beam spot diameter versus frequency, following the method at the X-band reported in [39].

REFERENCES

[1] K. Yi, S.-W. Moon, I.-S. Lee, J.-Y. Um, and I. Moon, "Design of a full-range ACC with collision avoidacne/mitigation braking," *IFAC Proc. Volumes*, vol. 40, no. 10, pp. 127–134, 2007.

[2] Z. Sun, G. Bebis, and R. Miller, "On-road vehicle detection: A review," *IEEE Trans. Pattern Anal. Mach. Intell.*, vol. 28, no. 5, pp. 694–711, May 2006.

[3] J. Hasch, E. Topak, R. Schnabel, T. Zwick, R. Weigel, and C. Waldschmidt, "Millimeter-wave technology for automotive radar sensors in the 77 GHz frequency band," *IEEE Trans. Microw. Theory Techn.*, vol. 60, no. 3, pp. 845–860, Mar. 2012.

[4] M.-S. Kim and S.-S. Kim, "Design and fabrication of 77-GHz radar absorbing materials using frequency-selective surfaces for autonomous vehicles application," *IEEE Microw. Wireless Compon. Lett.*, vol. 29, no. 12, pp. 779–782, Dec. 2019.

[5] L. Maurer, G. Haider, and H. Knapp, "77 GHz SiGe based bipolar transceivers for automotive radar applications—An industrial perspective," in *Proc. IEEE 9th Int. New Circuits Syst. Conf.*, Bordeaux, France, Jun. 2011, pp. 257–260.

[6] M. Goppelt, H.-L. Blöcher, and W. Menzel, "Automotive radar–investigation of mutual interference mechanisms," *Adv. Radio Sci.*, vol. 8, pp. 55–60, Sep. 2010.

[7] D. C. Schleher, *Electronic Warfare in the Information Age*, London, U.K.: Artech House, 1999.

[8] S. A. Silva, J. J. Pereira, E. L. Nohara, and M. C. Rezende, "Electromagnetic behavior of microwave absorbing materials based on Ca hexaferrite modified with CoTi ions and doped with La," *J. Aerosp. Technol. Manage.*, vol. 1, no. 2, pp. 255–263, 2009.

[9] D. D. L. Chung, "Electromagnetic interference shielding effectiveness of carbon materials," *Carbon*, vol. 39, no. 2, pp. 279–285, Feb. 2001.

[10] M. H. Al-Saleh, W. H. Saadeh, and U. Sundararaj, "EMI shielding effectiveness of carbon based nanostructured polymeric materials: A comparative study," *Carbon*, vol. 60, no. 8, pp. 146–156, Aug. 2013.

[11] D. Balageas and P. Levesque, "EMIR: A photothermal tool for electromagnetic phenomena characterization," *Revue Générale de Thermique*, vol. 37, no. 8, pp. 725–739, Sep. 1998.

[12] V. V. Varadan, "Radar absorbing applications of metamaterials," in *Proc. IEEE Region 5 Tech. Conf.*, Fayetteville, AR, USA, Apr. 2007, pp. 105–108.

[13] D. M. Pozar, *Microwave Engineering*. Hoboken, NJ, USA: Wiley, 2012.

[14] L. D. C. Folgueras, M. A. Alves, and M. C. Rezende, "Development, characterization and optimization of dielectric radar absorbent materials as flexible sheets for use at X-band," in *IEEE MTT-S Int. Microw. Symp. Dig.*, Brasilia, Brazil, 2007, pp. 488–491.

[15] D. Bourreau, A. Peden, and S. Le Maguer, "A quasi-optical free-space measurement setup without time-domain gating for material characterization in the *W*-band," *IEEE Trans. Instrum. Meas.*, vol. 55, no. 6, pp. 2022–2028, Dec. 2006.

[16] Y. Zhai, Y. Zhang, and W. Ren, "Electromagnetic characteristic and microwave absorbing performance of different carbon-based hydrogenated acrylonitrile–butadiene rubber composites," *Mater. Chem. Phys.*, vol. 133, no. 1, pp. 176–181, Mar. 2012.

[17] B. G. M. Helme, "Measurement of the microwave properties of materials," in *Proc. IEE Colloq. Ind. Uses Microw.*, London, U.K., 1990, pp. 3/1–3/7.

[18] L. F. Chen, C. K. Ong, C. P. Neo, V. V. Varadan, and V. K. Varadan, *Microwave Electronics: Measurement and Materials Characterization*. Hoboken, NJ, USA: Wiley, 2004.

[19] A. R. Von Hippel, *Dielectric Materials and Applications*, vol. 2. Dedham, MA, USA: Artech House, 1954.

[20] J. Baker-Jarvis *et al.*, "Dielectric characterization of low-loss materials a comparison of techniques," *IEEE Trans. Dielectr. Electr. Insul.*, vol. 5, no. 4, pp. 571–577, Aug. 1998.

[21] J. Obrzut, C. Emiroglu, O. Kirillov, Y. Yang, and R. E. Elmquist, "Surface conductance of graphene from non-contact resonant cavity," *Measurement*, vol. 87, pp. 146–151, Jun. 2016.

[22] C. L. Pournaropoulos and D. K. Misra, "The co-axial aperture electromagnetic sensor and its application in material characterization," *Meas. Sci. Technol.*, vol. 8, no. 11, pp. 1191–1202, 1997.

[23] S. Mueller *et al.*, "Broad-band microwave characterization of liquid crystals using a temperature-controlled coaxial transmission line," *IEEE Trans. Microw. Theory Techn.*, vol. 53, no. 6, pp. 1937–1945, Jun. 2005.

[24] N. Williams, V. K. Varadan, D. Ghodgaonkar, and V. V. Varadan, "Measurement of transmission and reflection of conductive lossy polymers at millimeter-wave frequencies," *IEEE Trans. Electromagn. Compat.*, vol. 32, no. 3, pp. 236–240, Aug. 1990.

[25] S. Sahin, N. K. Nahar, and K. Sertel, "A simplified Nicolson–Ross–Weir method for material characterization using single-port measurements," *IEEE Trans. THz Sci. Technol.*, vol. 10, no. 4, pp. 404–410, Jul. 2020.

[26] F. Costa, M. Borgese, M. Degiorgi, and A. Monorchio, "Electromagnetic characterisation of materials by using transmission/reflection (T/R) devices," *Electronics*, vol. 6, no. 95, pp. 1–27, 2017.

[27] Z. Qamar, N. Aboserwal, and J. L. Salazar-Cerreno, "An accurate method for designing, characterizing, and testing a multi-layer radome for mm-Wave applications," *IEEE Access*, vol. 8, pp. 23041–23053, 2020.

[28] N. Vohra, L. R. Rodriguez-Aguilar, J. S. Batista, and M. El-Shenawee, "Free-space characterization of radar absorbing non-magnetic materials in the W-band," in *Proc. ARFTG*, San Antonio, TX, USA, Jan. 2020, pp. 26–29.

[29] M. S. Hilario *et al.*, "W-band complex permittivity measurements at high temperature using free-space methods," *IEEE Trans. Compon., Package., Manuf. Technol.*, vol. 9, no. 6, pp. 1011–1019, Jun. 2019.

[30] H. Ahmed, J. Hyun, and J.-R. Lee, "Development of scanning single port free space measurement setup for imaging reflection loss of microwave absorbing materials," *Measurement*, vol. 125, pp. 114–122, Sep. 2018.

[31] T. Ozturk, A. Elhawil, I. Uluer, and M. T. Guneser, "Development of extraction techniques for dielectric constant from free-space measured S-parameters between 50 and 170 GHz," *J. Mater. Sci. Mater. Electron.*, vol. 28, no. 15, pp. 11543–11549, Aug. 2017.

[32] T. Ozturk, O. Morikawa, İ. Ünal, and İ. Uluer, "Comparison of free space measurement using a vector network analyzer and low-cost-type THz-TDS measurement methods between 75 and 325 GHz," *J. Infr. Millim. THz Waves*, vol. 38, no. 10, pp. 1241–1251, Oct. 2017.

[33] C. E. Kintner, "Free-space measurements of dielectrics and three-dimensional periodic metamaterials," M.S. thesis, Dept. Elect. Eng., Univ. Arkansas, Fayetteville, AR, USA, 2017. Accessed: Dec. 19, 2017. [Online]. Available: https://scholarworks.uark.edu/etd/2557

[34] Z. Akhter and M. J. Akhtar, "Free-space time domain position insensitive technique for simultaneous measurement of complex permittivity and thickness of lossy dielectric samples," *IEEE Trans. Instrum. Meas.*, vol. 65, no. 10, pp. 2394–2405, Oct. 2016.

[35] A. M. Hassan, J. Obrzut, and E. J. Garboczi, "A *Q*-band free-space characterization of carbon nanotube composites," *IEEE Trans. Microw. Theory Techn.*, vol. 64, no. 11, pp. 3807–3819, Nov. 2016.

[36] V. V. Varadan, K. A. Jose, and V. K. Varadan, "*In situ* microwave characterization of nonplanar dielectric objects," *IEEE Trans. Microw. Theory Techn.*, vol. 48, no. 3, pp. 388–394, Mar. 2000.

[37] F. C. Smith, J. C. Bennett, and B. Chambers, "Methodology for accurate free-space characterisation of radar absorbing materials," *IEE Proc. Sci., Meas. Technol.*, vol. 141, no. 6, pp. 538–546, Nov. 1994.

[38] D. V. Blackham, "Free space characterization of materials," in *Proc. Antenna Meas. Techn. Assoc. Symp.*, vol. 15, 1993, pp. 58–60.

[39] D. K. Ghodgaonkar, V. V. Varadan, and V. K. Varadan, "Free-space measurement of complex permittivity and complex permeability of magnetic materials at microwave frequencies," *IEEE Trans. Instrum. Meas.*, vol. 39, no. 2, pp. 387–394, Apr. 1990.

[40] M. H. Umari, D. K. Ghodgaonkar, V. V. Varadan, and V. K. Varadan, "A free-space bistatic calibration technique for the measurement of parallel and perpendicular reflection coefficients of planar samples," *IEEE Trans. Instrum. Meas.*, vol. 40, no. 1, pp. 19–24, Feb. 1991.

[41] V. V. Varadan, R. D. Hollinger, D. K. Ghodgaonkar, and V. K. Varadan, "Free-space, broadband measurements of high-temperature, complex dielectric properties at microwave frequencies," *IEEE Trans. Instrum. Meas.*, vol. 40, no. 5, pp. 842–846, Oct. 1991.

[42] S. Chen, K. A. Korolev, J. Kupershmidt, K. Nguyen, and M. N. Afsar, "High-resolution high-power quasi-optical free-space spectrometer for dielectric and magnetic measurements in millimeter waves," *IEEE Trans. Instrum. Meas.*, vol. 58, no. 8, pp. 2671–2678, Aug. 2009.

[43] G. L. Friedsam and E. M. Biebl, "A broadband free-space dielectric properties measurement system at millimeter wavelengths," *IEEE Trans. Instrum. Meas.*, vol. 46, no. 2, pp. 515–518, Apr. 1997.

[44] A. Technologies, "Advanced calibration techniques for vector network analyzers," in *Modern Measurement Techniques for Testing Advanced Military Communications and Radars*, 2nd ed. Santa Clara, CA, USA: Agilent Technologies, 2006.

[45] A. M. Nicolson and G. F. Ross, "Measurement of the intrinsic properties of materials by time-domain techniques," *IEEE Trans. Instrum. Meas.*, vol. IM-19, no. 4, pp. 377–382, Nov. 1970.

[46] J. Baker-Javis, M. D. Janezic, J. H. Grosvenor, Jr., and R. G. Geyer, "Transmission/reflection and short-circuit line methods for measuring permittivity and permeability," Electromagn. Fields Division Electron. Elect. Eng. Lab., Nat. Inst. Standards Technol., Boulder, CO, USA, NASA STIRecon Tech. Rep. N 1992, 93, 1992, Art. no. 12084.

[47] B. P. Singh, P. Bharadwaj, V. Choudhary, and R. B. Mathur, "Enhanced microwave shielding and mechanical properties of multiwall carbon nanotubes anchored carbon fiber felt reinforced epoxy multiscale composites," *Appl Nanosci*, vol. 4, pp. 421–428, Apr. 2014.

[48] D. R. Smith, D. C. Vier, T. Koschny, and C. M. Soukoulis, "Electromagnetic parameter retrieval from inhomogeneous metamaterials," *Phys. Rev. E, Stat. Phys. Plasmas Fluids Relat. Interdiscip. Top.*, vol. 71, Mar. 2005, Art. no. 036617.

[49] N. Vohra, J. S. Batista, and M. El-Shenawee, "Characterization of radar absorbing materials at 75 GHz −90 GHz using free-space system," in *Proc. IEEE-APS/URSI*, Montreal, QC, Canada, Jul. 2020, pp. 5–10.

[50] V. V. Varadan and R. Ro, "Unique retrieval of complex permittivity and permeability of dispersive materials from reflection and transmitted fields by enforcing causality," *IEEE Trans. Microw. Theory Techn.*, vol. 55, no. 10, pp. 2224–2230, Oct. 2007.

[51] O. Luukkonen, S. I. Maslovski, and S. A. Tretyakov, "A stepwise Nicolson–Ross–Weir-based material parameter extraction method," *IEEE Antennas Wireless Propag. Lett.*, vol. 10, pp. 1295–1298, 2011.

Nagma Vohra (Student Member, IEEE) received the B.S. degree in electronics and communication engineering from Guru Nanak Dev University, Amritsar, India, in 2014, and the M.S. degree in communication engineering from the Vellore Institute of Technology, Vellore, India, in 2017. She is currently pursuing the Ph.D. degree in electrical engineering with the University of Arkansas, Fayetteville, AR, USA, with a focus on biological and nonbiological material characterization at microwave and millimeter-wave frequencies.

Magda El-Shenawee (Senior Member, IEEE) received the Ph.D. degree from the University of Nebraska–Lincoln, Lincoln, NE, USA, in 1991.

She has been a Professor of electrical engineering with the University of Arkansas, Fayetteville, AR, USA, since 2001. Her background is in electromagnetics, theory, measurements, and computational techniques. Her educational goals are promoting the online antenna courses for industry and the open electromagnetic laboratory for undergraduate students. She authored or coauthored more than 230 articles in refereed journals and conference proceedings. Her research interests include experimental terahertz imaging and spectroscopy, breast cancer imaging, image reconstruction algorithms, antennas design and measurements, computational electromagnetics, biopotentials, and biomagnetics of breast cancerous cells. Her current research focuses on terahertz imaging and spectroscopy of breast tumor's margins and on material characterization in the microwave, millimeter-wave, and terahertz frequency bands.